IOPscience iopscience.iop.org

Home Search Collections Journals About Contact us My IOPscience

Highly ordered nanopatterns on Ge and Si surfaces by ion beam sputtering

This article has been downloaded from IOPscience. Please scroll down to see the full text article.

2009 J. Phys.: Condens. Matter 21 224003

(http://iopscience.iop.org/0953-8984/21/22/224003)

View the table of contents for this issue, or go to the journal homepage for more

Download details:
IP Address: 129.252.86.83
The article was downloaded on 29/05/2010 at 19:56

Please note that terms and conditions apply.

IOP Publishing — Journal of Physics: Condensed Matter

J. Phys.: Condens. Matter **21** (2009) 224003 (17pp) doi:10.1088/0953-8984/21/22/224003

Highly ordered nanopatterns on Ge and Si surfaces by ion beam sputtering

B Ziberi, M Cornejo, F Frost and B Rauschenbach

Leibniz-Institut für Oberflächenmodifizierung e. V. (IOM), Permoserstraße 15, D-04318 Leipzig, Germany

E-mail: bashkim.ziberi@iom-leipzig.de

Received 8 January 2009
Published 12 May 2009
Online at stacks.iop.org/JPhysCM/21/224003

Abstract

The bombardment of surfaces with low-energy ion beams leads to material erosion and can be accompanied by changes in the topography. Under certain conditions this surface erosion can result in well-ordered nanostructures. Here an overview of the pattern formation on Si and Ge surfaces under low-energy ion beam erosion at room temperature will be given. In particular, the formation of ripple and dot patterns, and the influence of different process parameters on their formation, ordering, shape and type will be discussed. Furthermore, the internal ion beam parameters inherent to broad beam ion sources are considered as an additional degree of freedom for controlling the pattern formation process. In this context: (i) formation of ripples at near-normal ion incidence, (ii) formation of dots at oblique ion incidence without sample rotation, (iii) transition between patterns, (iv) formation of ripples with different orientations and (v) long range ordered dot patterns will be presented and discussed.

(Some figures in this article are in colour only in the electronic version)

1. Introduction

The sputtering of solid surfaces with low-energy ions can lead to material erosion, usually accompanied by surface topography modifications. For particular sputtering conditions, due to self-organization processes, these topographies can evolve into well-ordered ripple or dot nanostructures on the surface. The main advantage of the ion erosion method is the possibility to produce large-area nanostructured surfaces in a one-step process and the easy control of different process parameters.

Nanostructure formation is observed on different materials such as metals [1–8], crystalline and amorphous semiconductors [9–23], and other materials [24–26]. In the last few years, it has been reported about the formation of dot nanostructures on III/V (InP, GaSb, InAs, InSb) semiconductors under normal ion incidence or oblique ion incidence with sample rotation [20, 21, 23, 27]. The evolving structures revealed particular domains with hexagonal ordering. These investigations paved the way for further intensive studies in this field by also including other materials for nanostructuring.

The process of nanostructure formation itself is a complex interplay between sputtering, that leads to surface roughening, and different relaxation mechanisms, that act to smooth the surface. Indeed, this interplay depends on different sputtering parameters. Therefore, it is important to study their influence on the evolution of the surface topography not only to identify the dominant mechanisms, but also to find the process parameters that can influence formation, size, shape and lateral ordering of nanostructures. The use of Si and Ge as the materials for investigation is not only due to their importance for different technological applications, but also for being simpler one-component systems, making it easier to explore the processes behind the pattern formation. For example, during studies on III/V semiconductors, it came out that it is difficult to understand the process of pattern formation. One reason was that these two-component systems lead to preferential sputtering and the enrichment of the dot nanostructures with one component, for example with indium or gallium. Another reason for using Si and Ge was the lack of a systematic study, at the time the work was started, on the evolution of the surface topography during low-energy ion beam erosion at room temperature.

For Si nanostructuring, up-to-date studies under noble gas ion beam erosion can be described as follows: (I) the formation of ripple patterns at relatively high ion energies (typically above 20 keV) at room temperature or below. Under these conditions, ripples form at ion incidence angles ranging from

 © 2009 IOP Publishing Ltd Printed in the UK

35° and 65° with respect to the surface normal, with ripple wavelengths above 300 nm [28–30]. Upon ion bombardment, the target surface becomes amorphous. (II) Ripple patterns emerging at lower ion energies up to 2000 eV. However, here the surface topography depends on the temperature used. Ripples form at temperatures above 400 °C, ion energy 750 eV and ion incidence angles near 67° [18]. Under these erosion conditions the target surface remains crystalline. Other results show ripple formation at near-normal ion incidence angles (5°–25°) at 300–2000 eV and room temperature [19]. In this case the upper surface layer is amorphous. On the other hand, dot patterns have been observed for Si at normal ion incidence for ion energy of 1200 eV [22], but with a low degree of ordering. Other reports demonstrate the formation of dot nanostructures at grazing incidence with simultaneous sample rotation, with a higher lateral ordering and amplitude [23].

Concerning Ge, only a few reports about pattern formation during low-energy ion beam erosion exist, e.g. formation of ripple patterns under 1000 eV Xe^+ ion beam sputtering at temperatures ∼300 °C and ion incidence angle of 55° [13]. The surface of the forming ripples remains crystalline after ion bombardment. The present authors showed that nanostructure formation at room temperature is also possible on Ge surfaces [32], and later reports confirm these results [33]. In this context, new parameters governing the pattern formation process that play a crucial role on the evolution of the surface topography were found [34]. These so-called internal beam parameters are proved to be an extra degree of freedom for pattern formation during ion beam erosion responsible for many experimental observations.

In this review a summary of our work on pattern formation on Si and Ge surfaces during low-energy ion beam erosion, with broad beam ion sources, at room temperature will be given. Depending on the processing parameters a multitude of different topographies can evolve on the surface of these materials. Specifically, the role of ion incidence angle, ion energy, ion fluence and ion species will be addressed. Furthermore, some unique properties of broad beam ion sources, like the internal beam parameters on the evolution of the surface morphology, will be discussed. In this review only experimental results will be discussed without entering into different existing theoretical models about pattern formation that will be discussed in other review papers.

After a short introduction on ion-induced nanostructuring, the history of pattern formation and the up-to-date studies on Si and Ge surfaces given above, we will continue in section 2 with the description of the experimental set-up, with the main focus on the broad beam ion source used. Section 3 will contain a general overview of the emerging surface topography on Si and Ge and with respect to the specific role of ion incidence angle and ion mass. The influence of ion energy and erosion time on the formation, size and ordering of ripple and dot patterns on Si and Ge based on selected examples will be summarized in section 4. Section 5 is devoted to a detailed study of ion incidence angle and internal ion beam parameters, on the pattern formation and the transitions between different types of pattern. Also it will be shown that, by a proper adjustment of these parameters, a large scale lateral ordering of nanostructures is possible.

2. Experimental set-up

The experiments were performed on an ion beam etching facility (ISA150). The main parts are: (a) pumping system; (b) gas system for supplying sputter gases; (c) the load lock for sample handling; (d) Faraday cup arrays; (e) sample holder and (f) the ion source [35].

The base pressure in the chamber is about 2×10^{-6} mbar. Depending on the gas species used (Ne^+, Ar^+, Kr^+ and Xe^+), the working pressure was varied between 5×10^{-5} and 1×10^{-4} mbar in order to maintain the stable operation of the beam source. The distance between the sample holder and the ion source (acceleration grid) amounts to around 400 mm, and is smaller than the mean free path length of ions, which is around 1 m for the working pressure given above. Therefore the extracted ions will reach the sample without collisions that could affect their kinetic energy and lead to a broad beam. The sample holder offers the possibility of rotating around its axis at about 12 rotations $\min^{-1}$. Additionally, it can be tilted from 0° (corresponding to normal ion incidence) up to 90° with respect to the axis of the ion beam source. Further, to avoid thermal effects on the sample the back side of the sample holder is water cooled. The ion gun is a home-built broad beam source of Kaufman type with a two-grid ion optics system. All inner parts of the ion source are made of purified graphite. The ion optical system is made of two multi-aperture plane parallel grids with small holes (for the given diameter around 3000 holes) with a cylindrical form covering the whole grid surface. In order to have higher transparency the holes are hexagonally arranged. The grid system consists of the screen grid and the acceleration grid that are used to extract the ions from the plasma. The geometrical characteristics of the different grid systems used were: (a) hole diameters of 2.5 mm each; (b) hole circle diameters between 180 and 192 mm; (c) thickness of screen grid 1 mm, thickness of acceleration grid 2 mm; (d) the distance between grids is 2 mm. After the plasma is created the potential of the discharge anode is determined by the voltage applied at the screen grid U_{scr}. It is the anode voltage ($U_{\mathrm{dis}} + U_{\mathrm{scr}}$) that determines the ion beam energy, thereafter called the beam voltage U_{b}. By applying an appropriate negative voltage at the acceleration grid (U_{acc}), ions will be extracted from the plasma and accelerated toward the second grid. The total extraction voltage is given by the absolute values of U_{b} and U_{acc}, $U_{\mathrm{extr}} = U_{\mathrm{b}} - U_{\mathrm{acc}}$. Under experimental conditions the beam and accelerator grids can take values that vary between $100\ \mathrm{V} \leqslant U_{\mathrm{b}} \leqslant 2000\ \mathrm{V}$ and $-1000\ \mathrm{V} \leqslant U_{\mathrm{acc}} \leqslant -10\ \mathrm{V}$. This total voltage, together with the geometrical characteristics of the grid systems used, including the shape of the plasma sheath boundary at the screen grid, define the overall ion optical parameters of the source, i.e. the ion beam divergence and angular distribution of the ions within the beam, respectively [36]. These so-called internal ion beam parameters are inherent to all broad beam ion sources, typically used for low-energy ion beam sputtering, resulting in a non-ideally parallel ion beam, i.e. all ions forming the beam feature an angular distribution which is also reflected in the angular distribution of ions arriving at the surface. These parameters usually play a crucial role in the evolution of the surface topography, as will be shown later on.

Samples used were commercially available epi-polished Si(100) substrates (p-type, 0.01–0.02 Ω cm) and Ge(100) substrates (undoped, >30 Ω cm) with a root-mean-square (rms) roughness of ∼0.2 nm.

The surface topography was analysed using mainly imaging techniques like scanning force microscopy (AFM), scanning electron microscopy SEM and high resolution transmission electron microscopy HRTEM.

The AFM results presented have at least a resolution of 512 pixels × 512 pixels, and Si probes with (nominal) tip radii smaller than 10 nm were used. The surface roughness and pattern were quantitatively characterized by first-order and second-order statistical quantities. In particular, the rms (root mean square) roughness was taken to quantify the surface roughness and as a measure for amplitude variations of the patterned surfaces [37]. For the profound evaluation of the lateral correlation of self-organized structures (e.g. ordering and pattern analysis) the reciprocal space quantities, the discrete two-dimensional fast Fourier transformation (2D FFT) and the (angular averaged) power spectral density (PSD) have been utilized. In contrast to a dot pattern showing an isotropic distribution, in the case of ripples there is an anisotropic distribution of the spatial frequencies. However, by performing angular averaging of the FFT image, the dominating spatial frequencies (the spots) will contribute mostly to the PSD spectra compared to the rest of the Fourier spectrum [35]. The position of the first spot/ring (peak) in the FFT (PSD) determines the characteristic spatial frequency of ripples/dots, i.e. the wavelength of structures in the real space. From the width of the spot/ring (peak) information about the homogeneity and spatial correlation of periodicities can be deduced. Additional spots/rings (peaks) are multiples of the first one and are related to the high lateral ordering of structures. In fact, the position of the first spot/ring (peak) gives the mean separation between the structures. For the ripples, it is assumed that the separation between ripples is equal to the ripple periodicity, i.e. wavelength. For the dot pattern, the mean separation is equal to the mean lateral size by supposing that the dots are close packed to each other.

For quantitative analysis of the lateral ordering of nanostructures the system correlation length ζ is used. The ζ gives the length scale up to which spatial correlation is present, i.e. the mean domain size of nanostructures. It is deduced from the FWHM of the first-order PSD peak and is inversely proportional to the FWHM, $\zeta \sim 1/\,\mathrm{FWHM}$ [37].

At the end it should be stated that the experiments have been performed during a period of four years with more than 3000 samples sputtered. The reproducibility uncertainties in the determination of the wavelength (λ), surface roughness (rms) and the system correlation length (ζ) is in the range of 10% between different experimental runs, including grid erosion and lifetime effects that are specific to broad beam ion sources. Therefore we abstain from giving error bars for these quantities and discuss our results by considering a maximal deviation of 10% to the given values. Within different experimental runs the reproducibility is much less than 10%.

3. General overview: topography evolution under low-energy ion beam erosion on Si and Ge

As already mentioned in section 1 there are many parameters which play a crucial role for the formation of nanostructures on the surface, beginning with the geometrical parameters of the ion optical system, continuing with the extraction voltages applied on the grid system and ending with the parameters that influence the ion–target interactions. For the rest of the work, the experimental results concerning the influence of these parameters on the evolution of ripple and dot patterns on Si and Ge surfaces will be discussed.

In this section an overview of topographies emerging on Si and Ge surfaces will be given. In general, the role of ion incidence angle, sample rotation and ion species on the evolution of the surface topography will be put into focus.

During low-energy ion beam erosion of Si and Ge surfaces, different topographies can evolve on the surface. Features like holes, bumps, ripples and dots are common. An important role on the evolution of the surface topography, at oblique ion incidence angles, exerts the rotation, respectively non-rotation, of the target holder around its surface normal. In cases with sample rotation (SR), due to rotational symmetry, there is an isotropic evolution of the surface topography that, for certain conditions, can evolve into well-ordered dot nanostructures on the surface. For the case with no sample rotation (NSR) there is an anisotropy present on the surface given by the ion beam direction. In general, this results in the formation of structures (usually ripples) with preferred spatial orientation, related to the ion beam direction.

Examples of different topographies emerging during low-energy ion beam erosion of Si are given in figure 1. Si substrates were bombarded with Ar^+ ions, at ion energies $E_{\mathrm{ion}} \leqslant 2000$ eV, with an ion flux of $J = 1.87 \times 10^{15}$ cm^{-2} s^{-1} for 3600 s, corresponding to a total ion fluence of $\Phi = 6.7 \times 10^{18}$ cm^{-2}. The AFM images reveal a complexity of different topographies on the surface by varying the ion incidence angle α_{ion}. In the case of SR (figures 1(a)–(c)) topographies like hole structures, smooth surfaces or isotropically distributed dot structures form on Si. For the case with NSR (figures 1(d)–(f)), structures showing preferential orientation form on the surface, like ripples aligned perpendicular or columnar structures aligned along the ion beam projection, respectively. Similar erosion patterns are observed by using Kr^+ and Xe^+ ions to bombard the Si surface, and for Ge surfaces using Kr^+ and Xe^+ ions, especially in the case of NSR. The evolution of the surface topography is quantitatively analysed in terms of rms surface roughness w. These results are summarized in figure 2, where w is plotted as a function of α_{ion} for Ar^+ ion erosion of Si surfaces. The graph shows that the roughness decreases up to a minimum value with ion incidence angle. By further increase of α_{ion} the w increases again. Figure 2 reveals that the qualitative behaviour of the surface roughness with respect to α_{ion} is independent of the ion energy used and if there is sample rotation or not. In general, three regions with regard to α_{ion} can be distinguished. Region I: the surface is rough for α_{ion} between 0° and ∼40°, and features like dots, holes and ripples form on the surface. Region II: smooth surfaces for

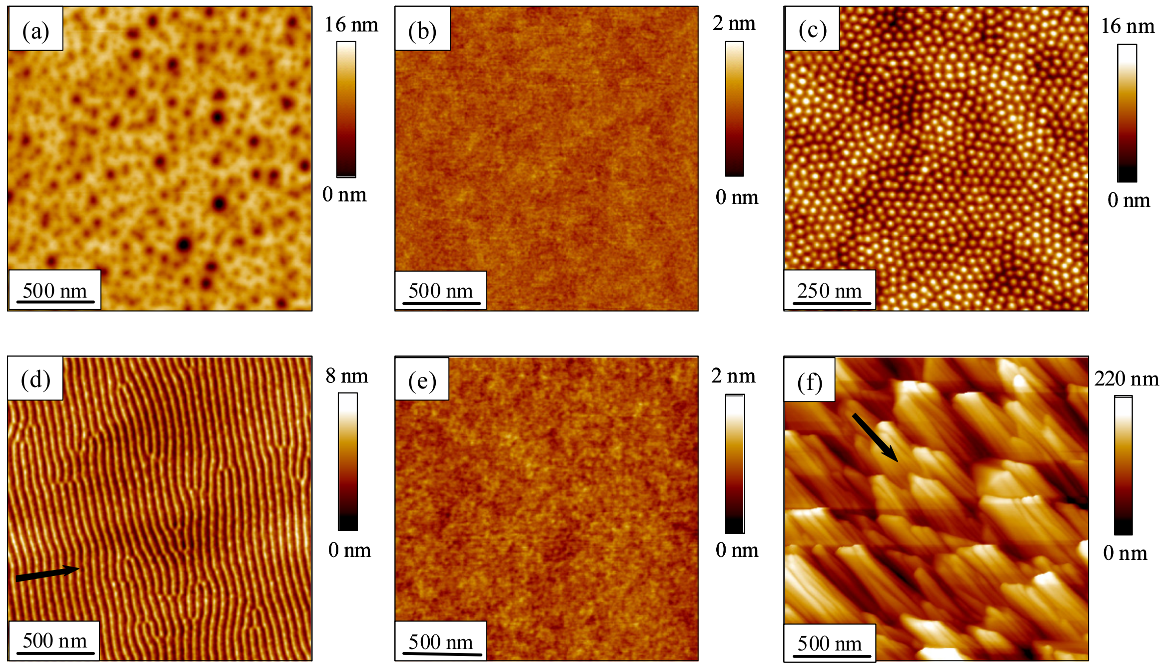

Figure 1. AFM images of different topographies on Si surfaces after Ar^+ ion beam erosion. The black arrow indicates the ion beam direction. (a)–(c) $E_{ion} = 500$ eV, sample rotation, (a) $\alpha_{ion} = 0°$, (b) $\alpha_{ion} = 45°$, (c) $\alpha_{ion} = 75°$. (d)–(f) $E_{ion} = 1500$ eV, no sample rotation, (d) $\alpha_{ion} = 15°$, (e) $\alpha_{ion} = 45°$, (f) $\alpha_{ion} = 5°$.

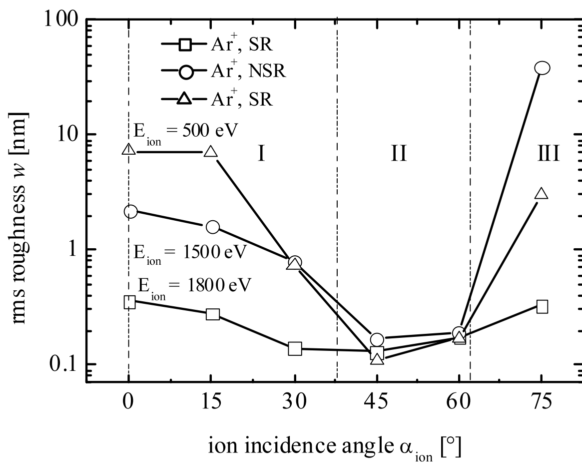

Figure 2. Development of rms surface roughness with ion incidence angle for Si at different ion energies. The results are plotted for the case with SR and with NSR.

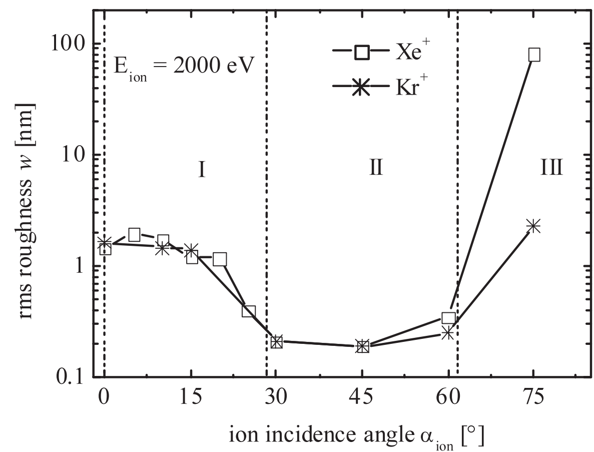

Figure 3. Rms surface roughness w as a function of α_{ion} using Kr^+ and Xe^+ ions to bombard the Ge surface at $\Phi = 6.7 \times 10^{18}$ cm^{-2}, $E_{ion} = 2000$ eV, without sample rotation.

α_{ion} from ~40° up to ~60°. Region III: the surface roughens again at grazing incidence above 60° and features like dots or columnar structures emerge. Analogous results are obtained using different ion species, like Kr^+ and Xe^+ ions, to bombard the Si surface. Figure 3 shows a similar behaviour for the evolution of the surface roughness, and hence of the surface topography, with ion incidence angle on Ge surfaces using Kr^+ and Xe^+ ions.

There is a parameter region for both materials with its centre at 45° where the surface remains stable, independent of all the other sputtering parameters used in this work. Namely, at this ion incidence angle the surface remains smooth with a roughness $w < 0.2$ nm. Hence, this sputtering condition is very well suited for large-area surface smoothing and finds a broad application in the field of optical manufacturing [38–40].

Experimental results clearly show that the evolution of the surface topography on Si and Ge surfaces is ion-species-dependent. When an ion penetrates the target surface it transfers its energy and momentum due to collision processes to the target atoms until it comes to rest. This process of the slowing down of ions gives rise to different phenomena on the surface and near-surface regions. The most important parameters are the range and straggling of the distribution of the deposited energy of incoming ions. This distribution

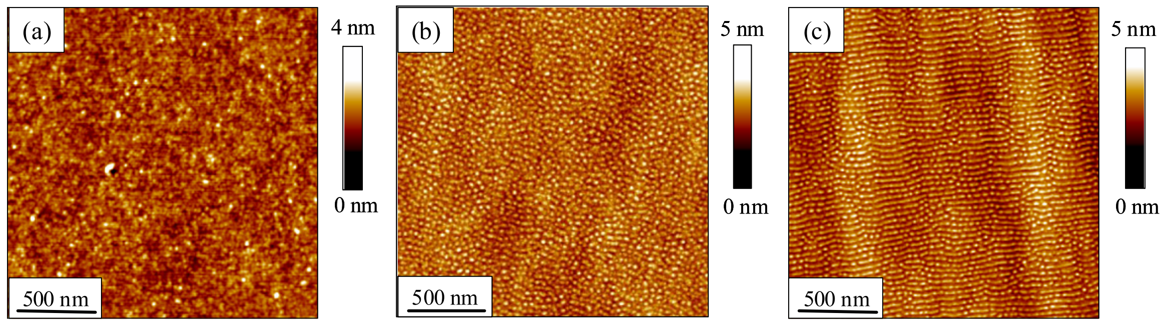

Figure 4. Surface topographies on Ge after ion beam erosion with different ion species at $E_{ion} = 1200$ eV and $\alpha_{ion} = 15°$ without sample rotation. (a) Ar^+, (b) Kr^+, (c) Xe^+.

depends on the energy of incoming ions, ion incidence angle and the properties of the target material. Additionally, the distribution depends on the mass of the incoming ions.

During the bombardment of Si surfaces with Ne^+ ions at ion energies 300 eV $\leqslant E_{ion} \leqslant$ 1000 eV structures evolve on the surface. For 1000 eV $\leqslant E_{ion} \leqslant$ 2000 eV the surface remains smooth[1]. Using Ar^+, Kr^+ and Xe^+ as bombarding ions the surface roughens i.e. structures evolve. A similar dependence of the surface topography on Si with different ion species was observed previously by Carter for intermediate ion energies (above 20 keV) [41]. In the case of Ge, no structures are commonly observed (the surface remains smooth) when Ne^+ and Ar^+ ions are used to bombard the surface. An example of topography evolution on Ge surfaces for different ion species is given in figure 4. The AFM images show that, in the case of Ar^+ ions, the surface remains smooth, while for Kr^+ and Xe^+ ions a dot-like structure evolves on the surface. However, there is a region (E_{ion} = 1300–2000 eV and α_{ion} = 0°–20°) where dot-like structures are also observed using Ar^+ ions, but with no ordering and an amplitude below 1 nm.

Due to the lack of experimental and theoretical studies, up to now, on the influence of ion species on the surface topography on Si and Ge, it is difficult to give an exact explanation for the above observations. Nevertheless, two possible explanations may be considered. (i) The first one is related to the distribution of the energy deposited by the incoming ions to the target surface atoms that depends on the mass of the ions. Calculations, supported by simulations using the SRIM code [42], show that, with increasing ion mass, the mean penetration depth and the width of the distribution decrease [35].

This means that, for heavier ions, the energy distribution maximum is located closer to the surface region than for lighter ions, i.e. more recoils are created in the upper surface layer for heavier ions [43]. (ii) The second explanation is related to the highly energetic sputtered target atoms as well as backscattered projectile ions originating during the sputtering process. These sputtered particles contribute to the additional sputtering of peaks compared to valleys, hence prohibiting the evolution of structures and leading to smooth surfaces [44].

[1] For ion energies 300 eV $\leqslant E_{ion} \leqslant$ 1000 eV the formation of structures depends on other sputtering parameters, like the ion incidence angle. Contrary to this, for 1000 eV $\leqslant E_{ion} \leqslant$ 2000 eV the surface remains smooth, independent of the ion incidence angle.

In conclusion, the evolution of the surface topography in terms of surface roughness as a function of ion incidence angle was discussed without a detailed treatment of the particular structures. It was shown that there is a general behaviour of the surface roughness with ion incidence angle for different sputtering parameters. The experimental results show an obvious dependence of the surface topography on the ion species used. For ion species with lighter mass than the target, usually no structures are observed. On the other hand, once these structures form, their characteristics like periodicity, lateral ordering, homogeneity and height do not depend on the ion species used. Obviously, it is difficult and beyond the scope of this work to study the influence of different process parameters on all topographies presented in figure 1. In particular, as will be shown in the topography diagrams in the next sections, by varying the sputtering conditions additional structures evolve on the surface. Therefore, particular interest will be paid to ripple and dot structures, and hence to the conditions under which these structures evolve. A more detailed discussion of region I of figure 3 will be given in section 5.

4. Highly ordered ripple and dot patterns

In this section a detailed discussion of main parameters determining formation, structure size and ordering of patterns will be given. The focus will be on the formation of well-ordered ripples and dot nanostructures on the surface. Theoretically, the process of pattern formation is related to the competition between the curvature-dependent sputtering and different relaxation processes resulting in the formation of nanostructures on the surface. The question that arises is: is it possible to control the evolution, lateral ordering and size of structures? If yes, which parameters are more relevant? To answer this question the influence of different process parameters has to be addressed. Some of these parameters include the ion energy E_{ion}, ion fluence Φ and ion species. Section 4.1 will deal with the role of ion energy on the evolution of the surface topography. It will be shown that with increasing ion energy the wavelength of structures increases. However, there are conditions under which a completely new behaviour of the surface topography is observed, namely a change in orientation of the wavevector of ripples on Si, or

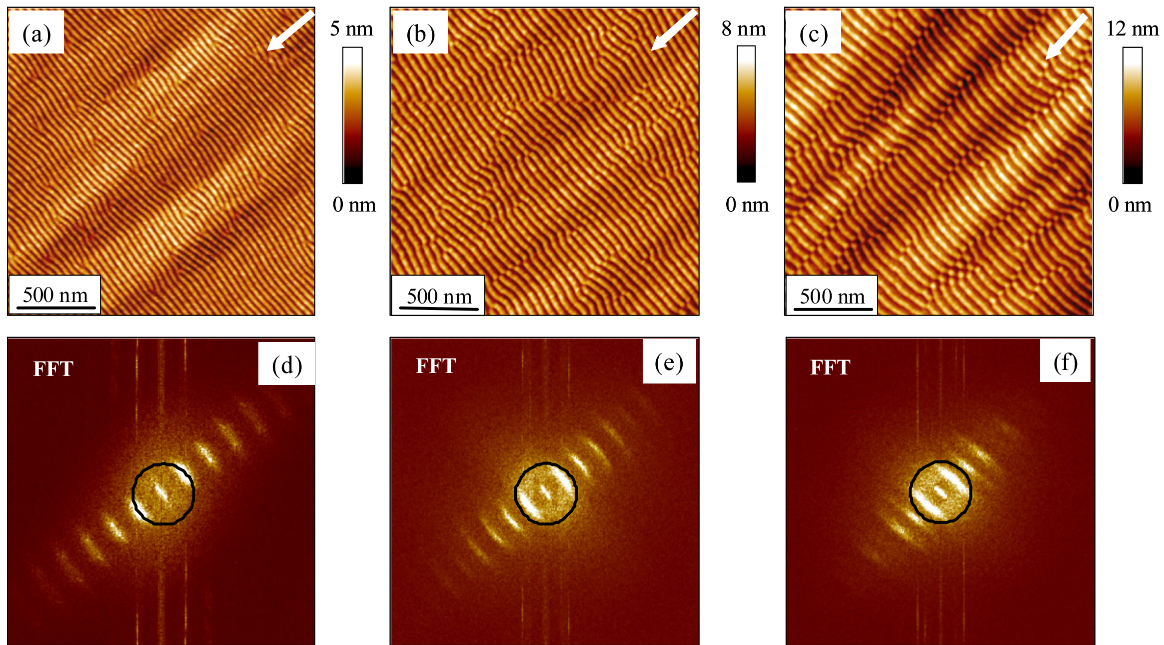

Figure 5. AFM images of self-organized ripple patterns on Si surfaces after Ar^+ ion beam erosion at $\alpha_{ion} = 15°$ for different ion energies. (a) $E_{ion} = 800$ eV, (b) $E_{ion} = 1200$ eV, (c) $E_{ion} = 2000$ eV. (d)–(f) Corresponding Fourier images (image size $\pm 128\ \mu m^{-1}$). The arrows indicate the direction of the incoming ion beam.

a transition from ripples to dots on Ge, with increasing ion energy. In section 4.2, the role of ion fluence on the evolution of the surface topography and the lateral ordering of structures will be discussed. While the wavelength of structures remains constant with ion fluence the lateral ordering increases.

Results for both materials, Si and Ge, are presented. In the case of Si, results will be given for Ar^+, Kr^+ and Xe^+ ions with and without sample rotation. In the case of SR the dot pattern formed under an ion incidence angle of 75° will be addressed [23]. For Ge only the case with NSR will be discussed. Dot structures form also on Ge surfaces with SR. However, under experimental conditions used in this work, they show only a poor lateral ordering and a large size distribution, making it very difficult to deduce general statements.

4.1. Role of ion energy

This section is devoted to the role of ion energy E_{ion} on the formation of dot and ripple patterns on Si and Ge surfaces. E_{ion} is varied between 500 and 2000 eV, which is limited by the power supply of the ion source. The experiments were performed at room temperature with an ion current density $j_{ion} \sim 300\ \mu A\ cm^{-2}$ (corresponding to an ion flux $J = 1.87 \times 10^{15}\ cm^{-2}\ s^{-1}$) and a total ion fluence of $\Phi = 6.7 \times 10^{18}\ cm^{-2}$. The ion fluence used ensures that the evolving patterns are well above the saturation regime concerning the surface roughness which will be discussed in this section.

In figure 5, the AFM images of ripple patterns emerging on Si surfaces, at $\alpha_{ion} = 15°$, without sample rotation are given. The Si surface is bombarded with Ar^+ ions with three different E_{ion}. The FFT images show clear multiple spots in the spatial-frequency spectra that correspond to the dominating ripple wavelength in real space and the high lateral ordering of ripples, respectively. The wavevector of ripples is parallel to the projection of the ion beam onto the surface plane. Compared to high spatial-frequency ripples, AFM images reveal additional low spatial-frequency corrugations on the surface with a wavevector perpendicular to the ion beam projection. Due to a rather broad size distribution, it is difficult to determine their wavelength. However, the amplitude of these corrugations is usually small compared to that of short wavelength ripples. The change of ripple wavelength λ and the normalized system correlation length ζ/λ with ion energy for Ar^+ and Kr^+ ion beam erosion are quantitatively summarized in figure 6. The graphs show an increasing λ from 40 up to 70 nm by varying the ion energy from 500 up to 2000 eV. The ratio ζ/λ shows for how many periods a perfect lateral ordering of ripples is present. While for Kr^+ ions the ordering of ripples is independent of E_{ion}, for Ar^+ ions the best ordering is achieved at $E_{ion} = 1200$ eV.

In the case of sample rotation the dot pattern can form at 75° ion incidence. In contrast to dot patterns forming at normal ion incidence [23] (similar to those reported by other research groups [22]) these dot patterns show a larger amplitude and a much better lateral ordering, making them more appropriate for our investigations. Figure 7 shows a typical example of dot patterns evolving on the Si surface during sputtering with Kr^+ ions at $E_{ion} = 1000$ eV. The AFM image shows domains of close packed, hexagonally ordered dot structures. These domains are randomly ordered with respect to each other which is reflected in the FFT image showing a ring.

Quantitatively, the dependence of λ and ζ/λ on E_{ion} for Ar^+, Kr^+ and Xe^+ ion beam erosion is summarized in figure 8. The results show an increase of the mean dot size, from 25 up to 50 nm, with increasing ion energy. Using Ar^+ ions, the

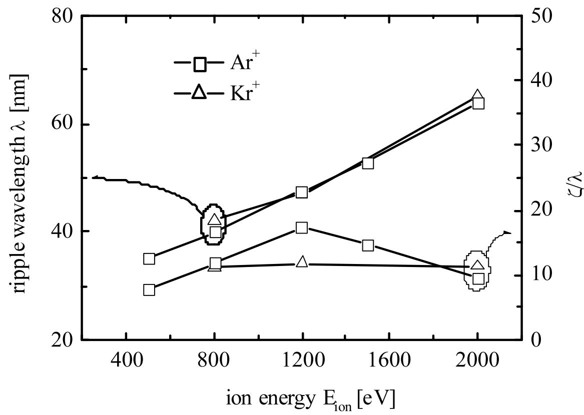

Figure 6. The dependence of the ripple wavelength λ and the system correlation length ζ (normalized to λ) on ion energy E_{ion} ($\alpha_{\text{ion}} = 15°$, Ar^+ and Kr^+ ions) for Si.

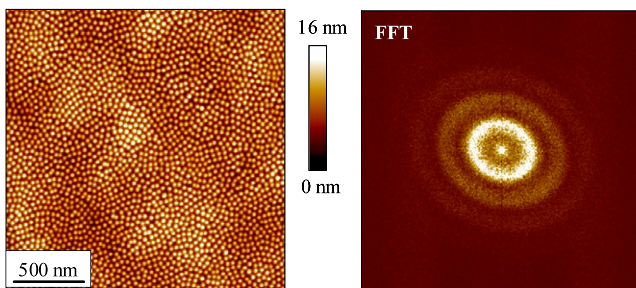

Figure 7. AFM image of dot structures on Si after Kr^+ ion beam erosion with SR at $E_{\text{ion}} = 1000$ eV and $\alpha_{\text{ion}} = 75°$. The corresponding FFT image (size $\pm 128\ \mu m^{-1}$), with clear distinct rings representing the periodicity and the lateral arrangement of dots.

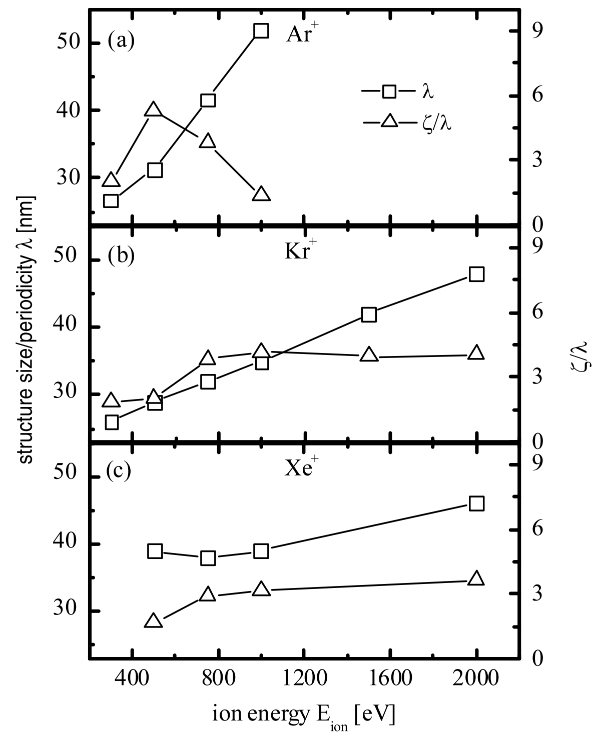

Figure 8. Variation of the mean dot size and normalized correlation length on Si with ion energy for different ion species.

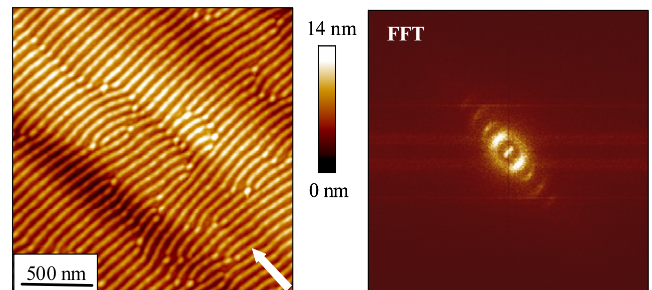

Figure 9. AFM image of ripple patterns on Ge surfaces after Xe^+ ion beam erosion, at $E_{\text{ion}} = 2000$ eV and $\alpha_{\text{ion}} = 5°$ without sample rotation. The arrow indicates the projected ion beam direction.

mean dot size increases up to $E_{\text{ion}} = 1000$ eV. For further increase in E_{ion}, dots start to overlap and form conglomerates of dots with no ordering, until at $E_{\text{ion}} = 2000$ eV the surface smoothens. For Kr^+ and Xe^+ ions, dots form in the range 500 eV $\leqslant E_{\text{ion}} \leqslant$ 2000 eV and their size increases with E_{ion}. The determination of the mean dot size for Xe^+ ions at $E_{\text{ion}} = 500$ eV is associated with a large uncertainty due to the marginal lateral ordering of dots. The ratio ζ/λ shows that, for $E_{\text{ion}} > 750$ eV, the lateral ordering of dot structures remains constant. For Ar^+ ions the best lateral ordering of dots is obtained at $E_{\text{ion}} = 500$ eV. Similar behaviour to that of Ar^+ is observed for Ne^+ ions under the given sputtering conditions. However, the uniformity and ordering of dots is much less pronounced than for Ar^+ ions.

Analogous investigations for the evolution of the surface topography with ion energy were performed for Ge. The parameters used for the sputtering process are identical to those for Si. A representative example of ripple patterns on Ge is given in figure 9 showing a surface after Xe^+ ion beam sputtering with $E_{\text{ion}} = 2000$ eV. The dependence of λ on E_{ion} is summarized in figure 10. The ripple wavelength increases with ion energy, similar to Si. For the given sputter conditions, no ripples were observed at $E_{\text{ion}} = 500$ eV. The ratio ζ/λ shows that for $E_{\text{ion}} > 1000$ eV the lateral ordering of ripples is improved significantly compared to $E_{\text{ion}} = 800$ eV.

Overall it was found that the evolution of the surface topography with E_{ion} in its entirety is more complex. To further illustrate this, AFM images of Si surfaces after sputtering with Xe^+ ions, at $\alpha_{\text{ion}} = 20°$, without sample rotation, for different ion energies are given in figure 11. For $E_{\text{ion}} = 1200$ eV ripple patterns with the wavevector parallel to the ion beam projection (parallel mode ripples) form on the surface with wavelength $\lambda = 46$ nm (figure 11(a)). By decreasing the ion energy to $E_{\text{ion}} = 800$ eV, ripples vanish and the surface remains smooth (figure 11(b)). Further decrease of ion energy results in a new type of ripple evolving on the surface as shown in figure 11(c). Now, the wavevector is oriented perpendicular to the ion beam projection (perpendicular mode ripples). These ripples have a mean height similar to ripples with parallel wavevector, but with wavelength $\lambda = 111$ nm, which is more than two times larger. The ion energy range where smooth surfaces occur is also affected by the respective ion incidence angle, e.g. it can be shifted toward smaller E_{ion} values with increasing α_{ion}.

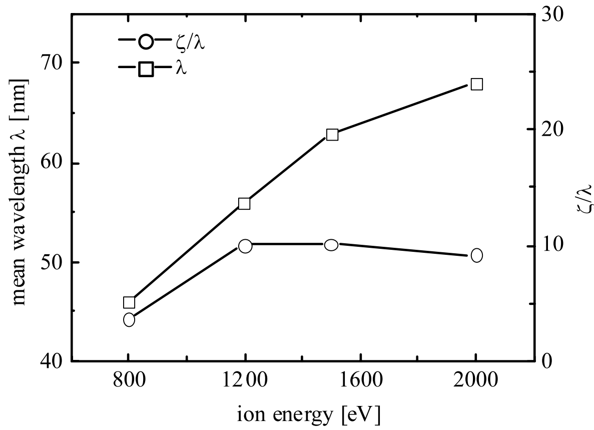

Figure 10. The dependence of λ and ζ/λ on E_{ion} for Xe^{+} ion beam erosion of Ge.

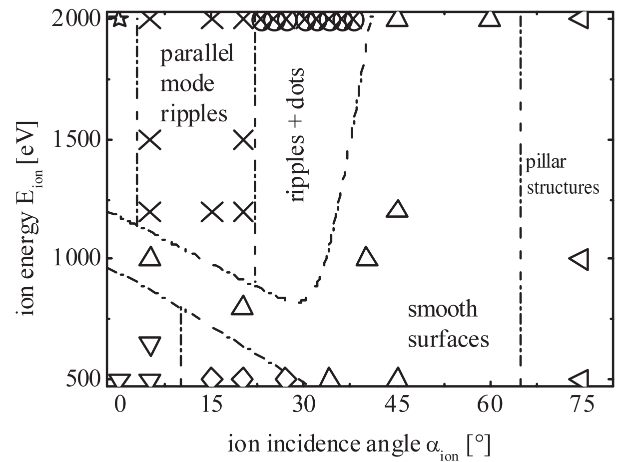

Figure 12. Topography diagram giving the surface topography on Si due to Xe^{+} ion beam erosion for different ion energies and ion incidence angles, without sample rotation. The symbols indicate the experimental data. △—smooth surfaces, ▽—hole structures, ✫—hillock structures, ◊—perpendicular-mode ripples, ⊗—parallel-mode ripples + dots, ×—parallel-mode ripples, ◁—columnar structures.

As an adequate representation, the evolution of the surface topography with different E_{ion} and α_{ion} are plotted in a so-called *topography diagram* (TD). Such a TD is presented in figure 12. Each symbol represents a typical topography. It reveals the different evolving topographies that depend on E_{ion} and α_{ion}. The boundaries (doted lines) on the TD are used as a guide for the eye, to distinguish between different topography regions. In most of the cases their position is taken as the midpoint between the experimental data representing two different topographies[2].

An analogous topography diagram was obtained for the Xe^{+} ion beam erosion of Ge (figure 13). The TD again gives a complex picture of evolving topographies. For $\alpha_{\mathrm{ion}} = 5°$ a transition from perpendicular-mode to parallel-mode ripples, or at $\alpha_{\mathrm{ion}} = 15°$ a transition from ripples to dots, is observed with increasing ion energy.

The above results for Si and Ge show that ion energy is a key parameter for pattern formation, and for determining their wavelength. Generally, the results show an increase of the wavelength of nanostructures and their amplitude with ion energy.

[2] This is done with the supposition that topographical transitions are continuous and that the transition point lies in the middle between the experimental data.

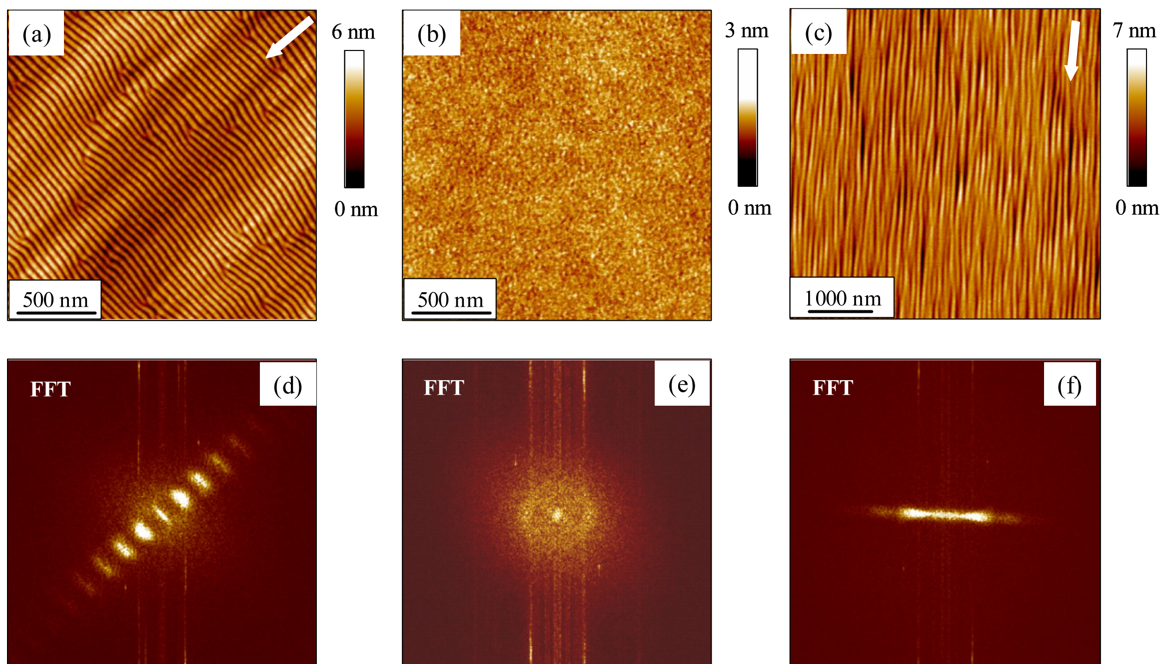

Figure 11. (a)–(c) Surface topography on Si after Xe^{+} ion beam sputtering at $\alpha_{\mathrm{ion}} = 20°$ for (a) $E_{\mathrm{ion}} = 1200$ eV, (b) $E_{\mathrm{ion}} = 800$ eV, (c) $E_{\mathrm{ion}} = 500$ eV. (d)–(f) Calculated FFT images with image size $\pm 128\ \mu m^{-1}$. Please note the different scale in AFM images.

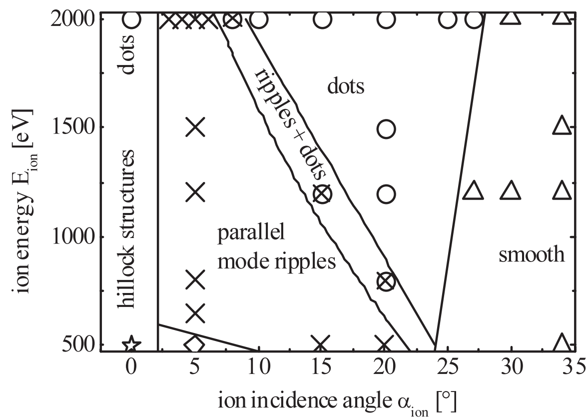

Figure 13. Topography diagram for Ge after Xe^+ ion beam sputtering for different ion energies and ion incidence angles. The symbols represent the experimental data: ☆—hillock structures, △—smooth surfaces, ◇—perpendicular-mode ripples, ⊗—parallel-mode ripples + dots, ×—parallel-mode ripples, ◁—columnar structures, O—dots.

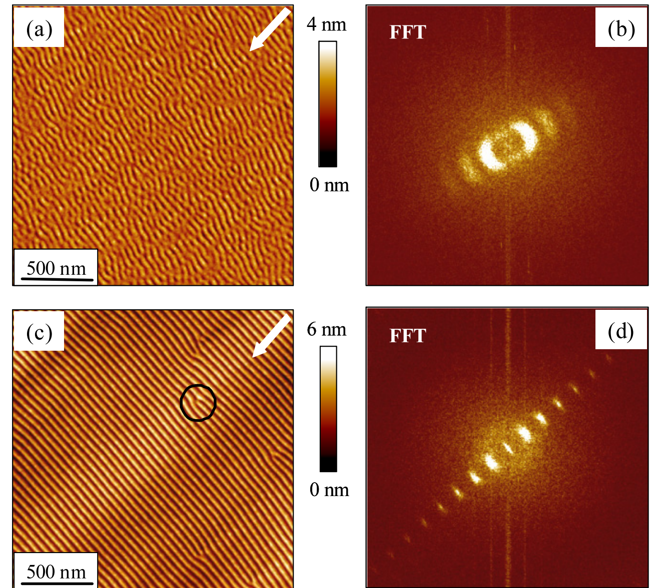

Figure 14. Surface topography on Si after Kr^+ ion beam erosion with $E_{ion} = 1200$ eV and $\alpha_{ion} = 15°$; (a) $\Phi = 3.4 \times 10^{17}$ cm^{-2} (sputter time 180 s), (c) $\Phi = 1.3 \times 10^{19}$ cm^{-2} (sputter time 7200 s). The solid circle in (c) indicates an existing defect between ripples. (b), (d) Corresponding Fourier images.

However, there are experimental conditions under which completely new phenomena are observed. One is the formation of perpendicular mode ripples with a wavelength approximately two times larger compared to the wavelength of parallel mode ripples. Moreover, there is a transition from ripples to dots with increasing ion energy on Ge surfaces. The topographical transition between different patterns with ion incidence angle will be further substantiated in 4.2.

4.2. *Time evolution of ripple and dot patterns*

In this section results about the evolution of the characteristic wavelength λ of nanostructures and the surface roughness w with erosion time (equivalent to the ion fluence Φ) for different ion species on Si and Ge will be presented. The ion fluence equals the total number of ions hitting the surface per unit area. For a given ion flux the ion fluence Φ is equivalent to the sputter time, or with the thickness of the removed layer. All experiments were conducted under conditions under which well-ordered ripple and dot structures are formed.

4.2.1. Wavelength evolution. A representative example of evolving ripple patterns, with increasing ion fluence on Si, is given in figure 14. The AFM image in figure 14(a) reveals a parallel-mode ripple topography from the beginning of the sputtering process with a distinct wavelength, as observed in the FFT image in figure 14(b). However, the rather broad radial and angular distribution of the first spot reveal that ripples have a rather poor lateral ordering (alignment) and size homogeneity. With increasing ion fluence the ordering of ripples increases (figures 14 (c) and (d)). The AFM image shows that ripples are interrupted by defects (denoted by the circle in figure 14(c)), producing two new ripples or coalescence of two ripples into one. The number of defects decreases with Φ, leading to almost perfectly ordered ripples with approximately 2 defects per 1 μm^2, shown in figure 14(c).

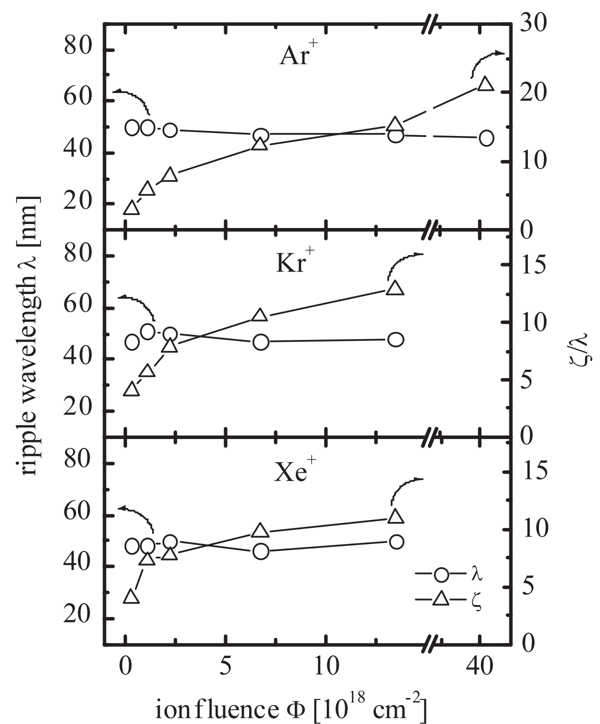

Figure 15. Ion fluence dependence of wavelength λ and normalized system correlation length ζ/λ for ripples on Si with $E_{ion} = 1200$ eV and $\alpha_{ion} = 15°$ for different ion species.

Quantitatively, the results for the evolution of λ and ζ/λ with ion fluence for Ar^+, Kr^+ and Xe^+ ion species are summarized in figure 15. The ripple wavelength of $\lambda \sim 50$ nm is constant while ζ/λ increases with ion fluence. At the beginning (up to an ion fluence $\Phi = 2 \times 10^{18}$ cm^{-2}) there

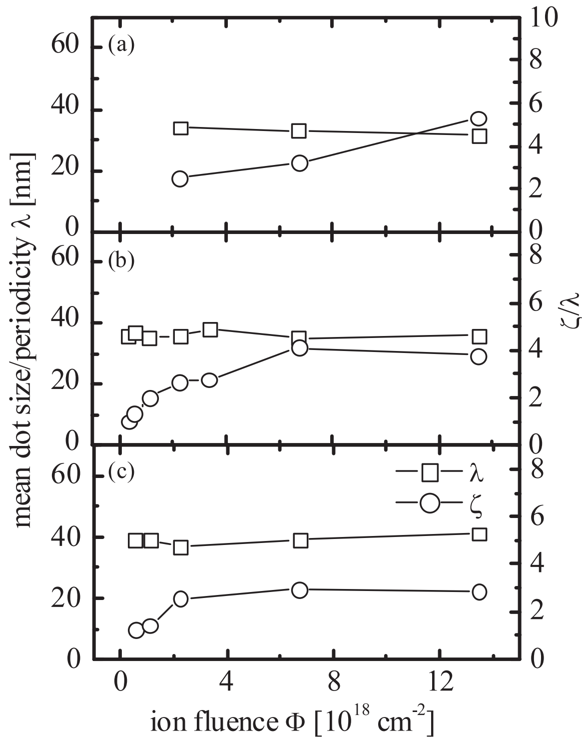

Figure 16. Dependence of λ and ζ/λ on ion fluence for dots on Si for $\alpha_{ion} = 75°$ with SR. (a) Ar^+, $E_{ion} = 500$ eV, (b) Kr^+, $E_{ion} = 1000$ eV, (c) Xe^+, $E_{ion} = 1000$ eV.

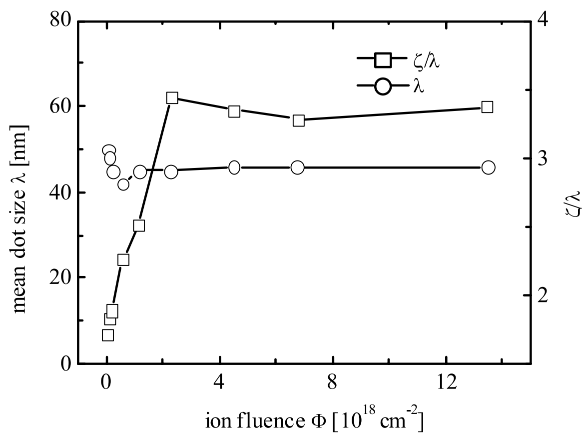

Figure 17. Evolution of mean dot size of λ and the normalized system correlation length ζ/λ with ion fluence, for dots on Ge with NSR ($\alpha_{ion} = 20°$, Xe^+, $E_{ion} = 2000$ eV).

is a steeper increase than for larger fluences. For a total fluence of $\Phi = 4 \times 10^{19}$ cm^{-2}, the ζ/λ extends above 20 periods. This value of the system correlation length for ripples can be interpreted as the mean distance between the defects on the AFM image.

Figure 16 shows the evolution of the mean size of dots λ and the normalized system correlation length ζ/λ with Φ at oblique ion incidence. The results are given for Ar^+ with $E_{ion} = 500$ eV (as shown in figure 8 for Ar^+ ion dots with the best lateral ordering evolve for $E_{ion} = 500$ eV) and Kr^+ and Xe^+ ions at $E_{ion} = 1000$ eV. From the graphs it can be seen

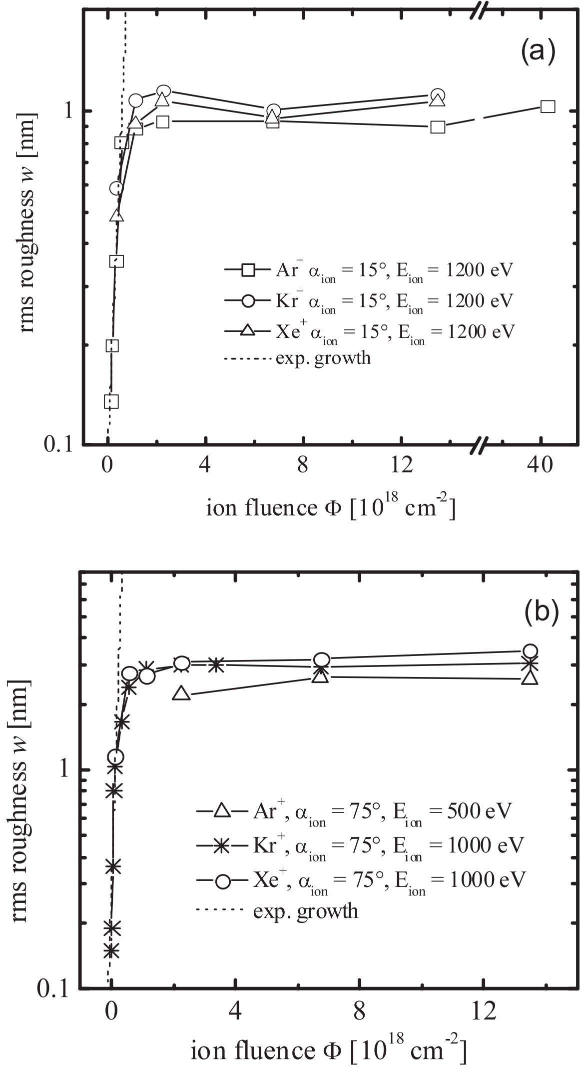

Figure 18. Rms surface roughness evolution with ion fluence in Si for different ion species: (a) ripples, (b) dots. The dotted line illustrates the exponential growth for the initial stage of sputtering.

that the mean size of dots does not change while the ratio ζ/λ increases with ion fluence. Further, the mean size of dots is nearly independent from the ion species used.

Similar results concerning the evolution of λ and ζ/λ with Φ for structures on Ge surfaces for the case without sample rotation are obtained (figure 17). The mean size fluctuations for low ion fluences are related to the large size distribution of dots, i.e. uncertainty in determining their mean size.

4.2.2. Time evolution of structure amplitudes. Finally evolution of the amplitude of ripple and dot structures for Si and Ge with ion fluence will be addressed. Experimental results presented in figure 18 for ripples and dots on Si show that, for small sputtering fluences up to 5.6×10^{17} cm^{-2}, w seems to grow exponentially (dotted line). For $\Phi \sim 1 \times 10^{18}$ cm^{-2}, the roughness, i.e. the ripple and dot amplitude, saturates and remains constant upon further sputtering. The results in figure 18 prove also that the evolution of the amplitude with ion fluence behaves similarly for Ar^+, Kr^+ and

Xe^+ ions and that there is a similar behaviour for ripples and dots.

A representative example for the evolution of surface height for Ge, using the same sputtering conditions as in figure 17, is given in figure 19. In this case the surface roughness saturates at an ion fluence of $\Phi = 8.4 \times 10^{16}$ cm^{-2}, corresponding to an erosion time of only 45 s.

Overall results for the temporal evolution of the structure amplitudes with ion fluence for the current density used can be summarized as follows: (i) for small ion fluences the surface roughness grows exponentially and (ii) with increasing ion fluence the roughness saturates and remains constant even for prolonged sputtering (up to $\Phi = 4 \times 10^{19}$ ions cm^{-2}). This means the amplitude of nanostructures saturates and remains constant for prolonged sputtering.

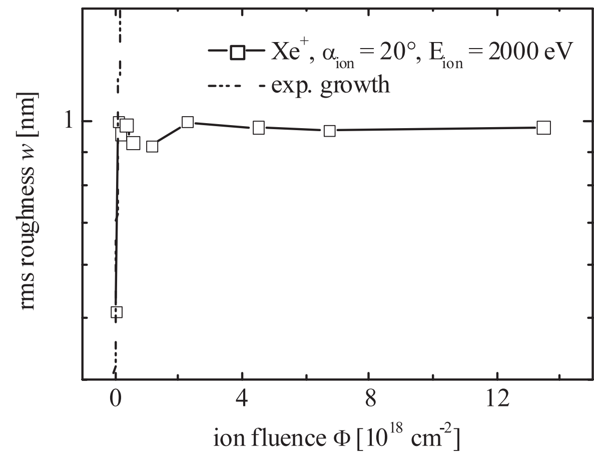

Figure 19. Evolution of rms surface roughness w with ion fluence Φ for Xe^+ ion beam erosion of Ge surfaces with no sample rotation.

5. Pattern transitions on Si and Ge surfaces

Experimental results presented in sections 3 and 4 proved the influence of different ion beam parameters on the evolution of the surface topography on Si and Ge. Particular attention was paid to the conditions where ripple and dot structures evolve. One of the main demands on these structures is to maintain a large scale lateral ordering. As will be shown in the next sections there are two parameters of the sputtering process that contribute significantly to the achievement of such ordering: these are the ion incidence angle and the internal ion beam parameters. In section 3, a general discussion of the role of ion incidence angle on the surface topography was given. However, small step variations of α_{ion} show a completely new phenomenon, i.e. a transition from ripple to dot pattern possessing a large scale ordering. This will be discussed in section 5.1. Section 5.2 will deal with the role of internal beam parameters inherent to broad beam ion sources, i.e. beam divergence and the angular distribution of ions within the ion beam. These quantities, neglected up to now in the studies for nanostructuring with ion beams, are found to play a crucial role in surface evolution processes. As pointed out from the topography diagrams in section 4 a diversity of structures can evolve depending on ion energy. Therefore in this section the ion energy will be kept constant at $E_{\mathrm{ion}} = 2000$ eV. Also the ion fluence used was fixed at $\Phi = 6.7 \times 10^{18}$ cm^{-2}, well above the saturation threshold for the pattern amplitude, with an ion current density $j_{\mathrm{ion}} \sim 300\ \mu$A cm^{-2}.

5.1. Role of ion incidence angle

It is well known that the energy deposited on the near-surface region of ions hitting the surface depends also on the incidence angle with respect to the surface normal. Therefore, it is expected that α_{ion} affects the surface topography. On the other side, α_{ion} is important in order to compare the experimental results with the theoretical models describing the process of ripple formation [45, 46]. Results in section 3 revealed that, depending on α_{ion}, topographies like dots, ripples and even smooth surfaces are possible. The amplitude development of ripples and dots on α_{ion} was divided mainly into three regions without discussing the transitions between these regions.

However, if one studies the evolution of the surface topography in more detail, i.e. for finer α_{ion} steps, the picture of the surface topography evolution is much more complex. Completely new topographies are observed, with a continuous transition from one type to the other. During this transition, there are α_{ion} values where the evolving structures are almost perfectly laterally ordered on a large scale, covering the entire sample. We start with a separate discussion for Si and Ge on the role of fine variations of the ion incidence angle in region I of figure 2. In the last part of this section the evolution of the wavelength of ripples and dots with α_{ion} for both materials will be discussed.

5.1.1. Influence of ion incidence angle on pattern transition on Si. Figure 20 shows examples of surface topographies evolving for different ion incidence angles for Xe^+ ion beam erosion with no sample rotation. For normal ion incidence the surface is smooth with small hillocks (figure 20(a)) in accordance with figure 12.[3] By changing the ion incidence angle to 5° with respect to the surface normal the topography changes completely (figure 20(b)) and well-ordered parallel mode ripple patterns evolve on the surface. By further increasing the ion incidence angle this topography remains stable up to $\alpha_{\mathrm{ion}} = 23°$, where a mixture of dots and ripples is observed on the surface as shown in figure 20(c). This mixed topography is preserved and with increasing α_{ion} the amplitude decreases until at $\alpha_{\mathrm{ion}} > 40°$ the surface smoothens (figure 20(d)). Below, the surface structures emerging around $\alpha_{\mathrm{ion}} = 23°$ will be analysed in detail. As figure 20(c) shows, dot and ripple structures form simultaneously on the surface. Ripples have a slightly curved form (compared to ripples at 5°) and are interrupted by dots. The dots themselves form mainly along the ripples, i.e. the alignment of dots is dictated by the previous alignment of ripples. By increasing the ion incidence angle to 25° this coexistence of patterns is retained (figure 21). However, a close look at the AFM

[3] In the case when Ar^+ ions are used to bombard the surface under normal incidence (not shown here) and dot structures appear similar to those reported by Gago *et al* [31].

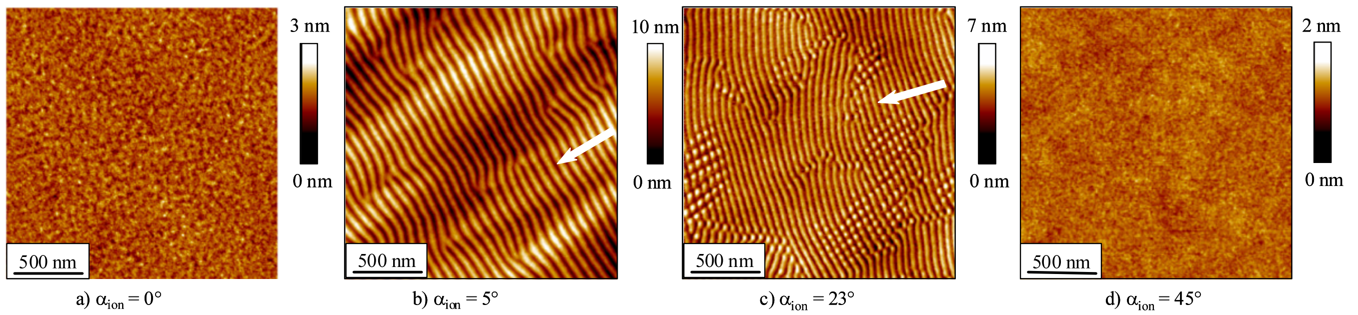

Figure 20. Surface topography on Si after Xe^+ ion beam erosion without sample rotation for different ion incidence angles. The arrows indicate the ion beam direction.

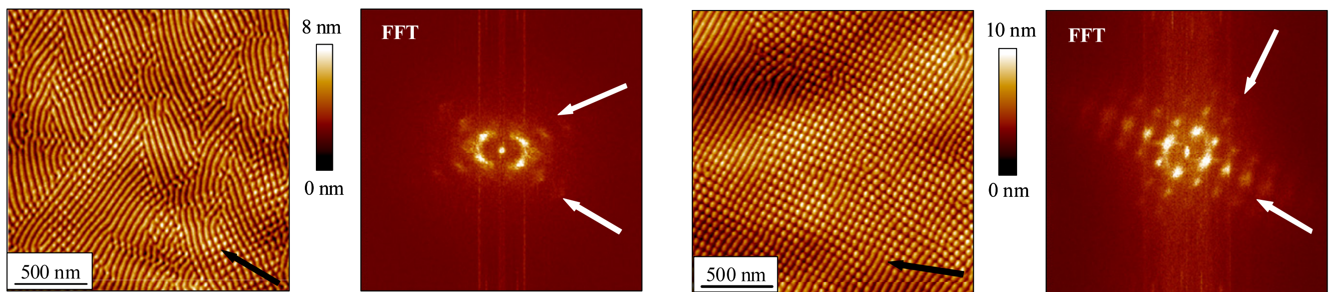

Figure 21. AFM image of coexisting ripple and dot structures on Si. The ripples have different orientations with respect to the ion incidence direction (the black arrow indicates the beam projection). Also given is the corresponding FFT image (white arrows point out the two distinct wavevectors).

Figure 22. An almost perfect square array of dots on an Si surface (Xe^+, $\alpha_{ion} = 26°$), where the black arrow indicates the ion beam direction. The corresponding FFT image confirms the square ordering of dots (white arrows point out the two distinct wavevectors).

image reveals that ripples with different spatial orientations form on the surface. From the AFM image mainly three types of ripples can be distinguished. The first type are aligned perpendicular to the ion beam projection. The second type of ripples make an angle different to the ion beam projection (the wavevector builds an angle of approximately 60° with the ion beam projection). The third type of ripples show a curved form. This is reflected also on the corresponding FFT image showing peaks with two distinct orientations. Additionally, the broad angular distribution of the first-order spots in the FFT, that possess a half-circle form, is due to the contribution of curved ripples observed by AFM. By further increase of α_{ion} to 26°, the AFM image shows structures aligned mainly in two directions that cross each other, making an angle of 90° between them (in the one direction some remaining ripples are still observed) (figure 22). It is interesting that both dominating directions are rotated with respect to the ion beam projection. i.e. they are neither perpendicular nor parallel to the ion beam projection. Along these directions dots having a chain-like form dominate the surface. The dots show an almost perfect lateral ordering, with only a few defects that are comparable to the defect density of ripples (see section 4). This is reflected in the corresponding FFT image, with the equidistant first-order spots implying the same periodicity of dots in the two directions and wavevectors perpendicular to each other.

5.1.2. Influence of ion incidence angle on pattern transition on Ge. The topography transition from ripples to dots is not only characteristic of Si but is also observed on Ge. However, for Ge there is first a transition from dots to ripples and then back from ripples to dots with increasing ion incidence angle. This can be seen from the surface evolution on Ge by Xe^+ ion beam sputtering at different ion incidence angles shown in figure 23. The AFM image for normal incidence in figure 23(a) shows dot structures whereas at $\alpha_{ion} = 5°$ the dot nanostructures disappear and well-ordered parallel mode ripples evolve on the surface (figure 23(b)). By increasing the ion incidence angle to 10° ripples, having a curved form, are still dominating the surface, but they start to transform into dots (figure 23(c)). Further increase of α_{ion} toward 20° results in a complete transition from ripple to dot pattern as shown in figure 23(d). The dots have a hexagonal ordering within the whole image area. The FFT image shows six equidistant peaks and it reveals that the ordering is more pronounced in the direction where previously ripples existed, as seen from the second-order peaks observed in the direction of the incoming beam. With further increase of α_{ion} the surface smoothens similar to Si.

For both materials the nanostructure wavelength λ decreases with α_{ion} as shown in figure 24 using Xe^+ ions. A similar behaviour is observed using Ar^+ and Kr^+ for Si and Kr^+ ions for Ge, indicating that the wavelength evolution is independent of the ion species used.

In summary, the results presented in this section indicate the importance of ion incidence angle on the evolution of the surface topography. Depending on ion incidence angle different topographies can evolve on the surface. In detail it

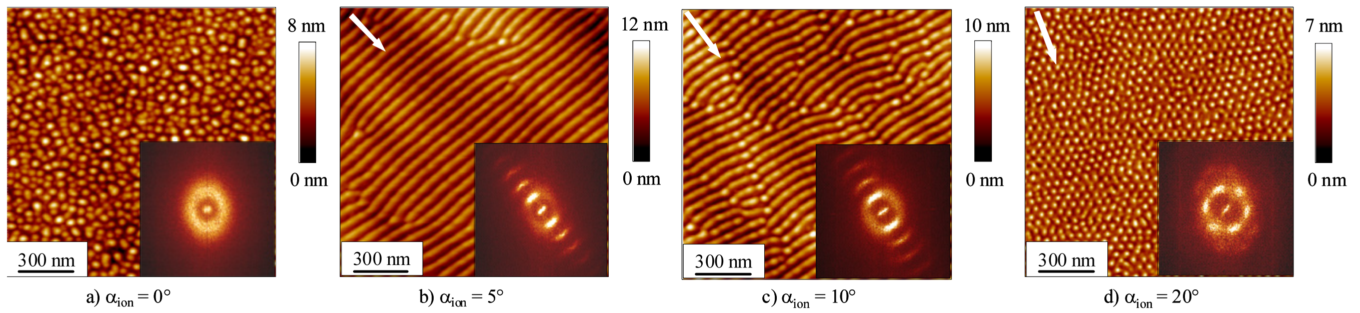

Figure 23. Surface topographies on Ge after Xe^+ ion beam erosion for different ion incidence angles. The arrows give the ion beam direction. Inset: corresponding FFT images calculated from AFM images having 4 μm × 4 μm size.

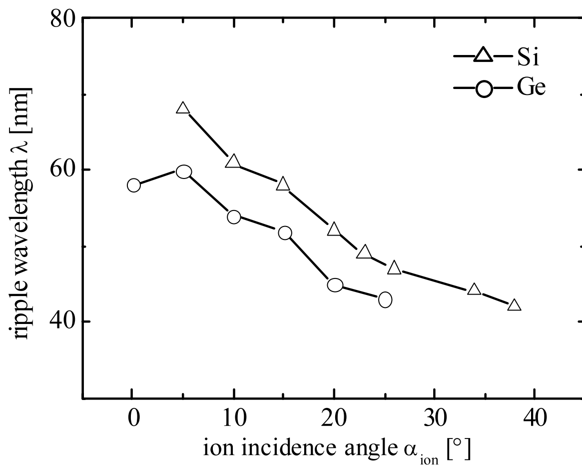

Figure 24. Experimental values of λ as a function α_{ion} using Xe^+ ions on Si and Ge surfaces.

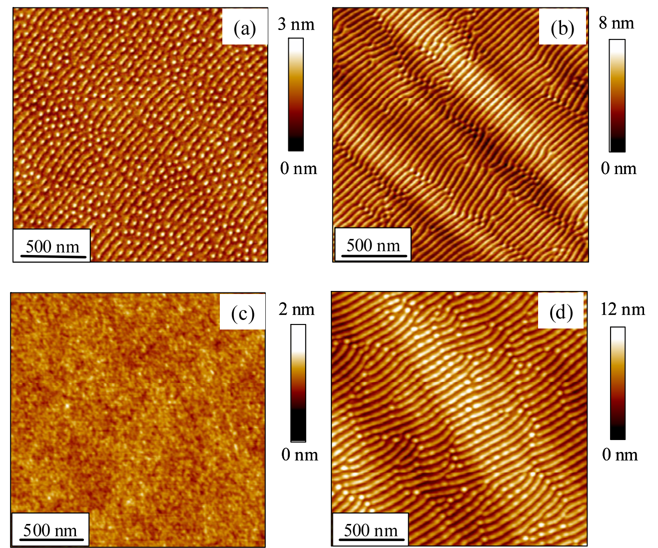

Figure 25. Surface topography on Si (a), (b) and Ge (c), (d) surfaces for different acceleration voltages during Xe^+ ion beam erosion without sample rotation at $E_{ion} = 2000$ eV: (a) $\alpha_{ion} = 20°$, $U_{acc} = -200$ V; (b) $\alpha_{ion} = 20°$, $U_{acc} = -1000$ V; (c) $\alpha_{ion} = 10°$, $U_{acc} = -200$ V; (d) $\alpha_{ion} = 10°$, $U_{acc} = -1000$ V.

was shown that:

(i) Ripple–dot transitions were found on Si and Ge surfaces caused by small variations of the ion incidence angle.
(ii) The transition is continuous and there are conditions at which a coexistence of both structures is possible. This coexistence remains even for large fluences, indicating that these mixed topographies are not *metastable*.
(iii) During the transition from ripples to dots, the former serve as a guide for the lateral ordering of dots.
(iv) Although there is a preferred orientation of the ion beam given by the ion incidence angle structures having hexagonal ordering evolve on the surface of Ge. Additionally, the dominant directions of laterally square ordered dots on Si are different from those of the ion beam projection.
(v) Ripples with different orientations compared to the direction of the projected ion beam form on the surface.
(vi) Ripple structures on both materials evolve at ion incidence angles just a few degrees off surface normal.

5.2. Role of internal beam parameters on the evolution of the surface topography

Based on these experiments, it is seen that fine variations in the incidence angle can have a strong effect on surface topography. In this regard, a further fundamental parameter governing the pattern formation process is identified. Inherent to all broad beam ion sources, typically used for low-energy ion beam sputtering, is a non-ideal parallel ion beam, i.e. all ions forming the beam have an angular distribution which is also reflected in the angular distribution of ions arriving at the surface. This so-called internal ion beam parameter, neglected up to now in all experimental studies and in theoretical models, plays a crucial role in the evolution of the surface topography. This angular distribution can be controlled by changing the voltages applied to the geometrically defined optical elements of the broad beam ion source introduced in section 2 [36, 47–52]. The voltage applied to the second grid (U_{acc}) mainly controls, in a well-defined range depending on the grid geometry as well as plasma parameters, the angular distribution under which the ions leave one aperture (the beam extracted from one aperture is named a beamlet) of the grid. The superposition of the individual beamlets forms the ion broad beam. Examples for the impact of U_{acc} on Si and Ge surfaces are given in figure 25. It substantiates that the spread in the local incidence angle caused by the angular distribution of ions within the broad beam may also influence the pattern evolution. In

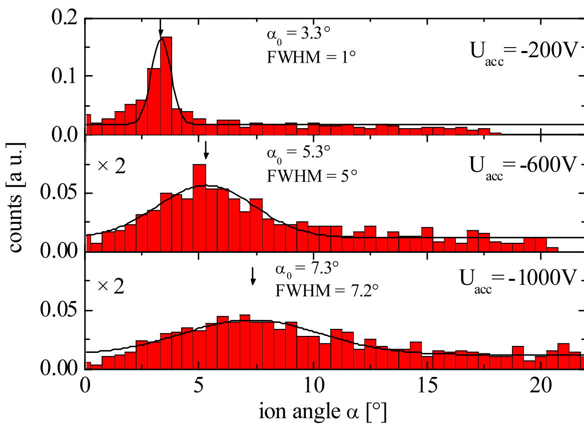

Figure 26. Angular distributions of ions leaving an aperture for different U_{acc} with $E_{ion} = 2000$ eV and a plasma density of $n_p = 2 \times 10^{10}$ cm^{-3}. The distributions are normalized to the total number of ions. The solid curves represent a Gaussian fit in order to deduce the maximum and the width of the distribution. The arrows indicate the position of the distribution maximum.

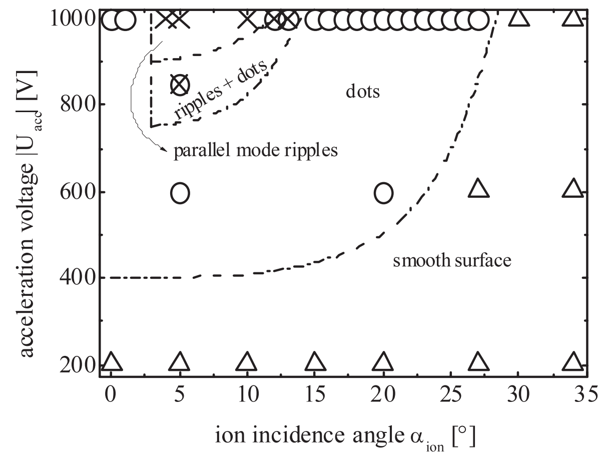

Figure 27. Topography diagram for Ge surfaces for different acceleration voltages U_{acc} and ion incidence angles α_{ion}. The presented results are for Xe^+ ions without sample rotation. The symbols represent the experimental data. △—smooth surfaces, ⊗—parallel-mode ripples + dots, ×—parallel-mode ripples, ○—dots.

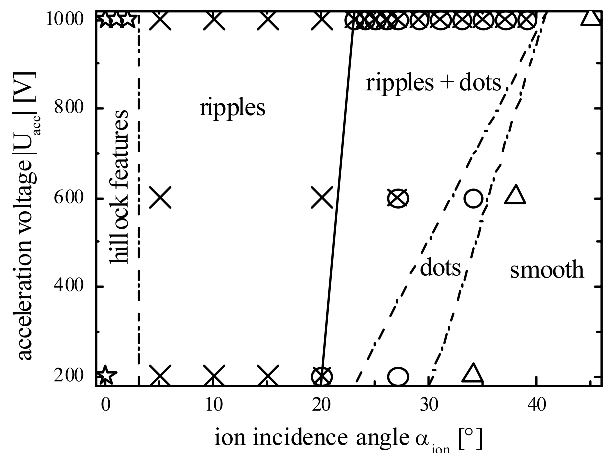

Figure 28. Topography diagram for 2000 eV Xe^+ ion beam erosion of Si surfaces for different acceleration voltages U_{acc} and ion incidence angles α_{ion}. The symbols denote different patterns obtained for different pairs of (α_{ion}, U_{acc}): ☆—hillock structures, ×—parallel-mode ripples, ⊗—parallel-mode ripples + dots, △—smooth surfaces, ○—dots.

detail, the angular distributions are analysed by performing simulations using the experimentally determined ion current density profiles as input data. The ion current density for different U_{acc} were measured by a 16 × 16 Faraday probe array and the simulations are realized using the computer code IGUN [53] with the specific geometrical dimensions of the ion optical system given in section 2. In figure 26, angular distributions of ions within a beamlet for different acceleration voltages are presented. Indeed, these simulations show that most of the ions leave the second grid not parallel to the ion beam axis. For $U_{acc} = -200$ V, the distribution shows a maximum at ∼3.3° with a full width at half-maximum (FWHM) of 1°, and most of the ions leave the aperture with an angle between 2° and 5°. With increasing absolute values of U_{acc}, the distribution broadens and the maximum shifts toward larger angles. For $U_{acc} = -1000$ V, these values change to 7.2° (maximum position) and 7.3°, respectively. Therefore, the spread of ions leaving the aperture becomes larger. Nevertheless, it must be pointed out that these values strongly depend on the particular ion source and ion extraction conditions.

The consequence of this ion beam parameter on the experimentally evolving pattern is summarized in the topography diagram in figure 27 for Ge. In addition to the influence of ion incidence angle by also varying the U_{acc} a topography transition can be obtained. This transition is, however, present only at a certain range of ion incidence angles. For example, for $\alpha_{ion} = 5°$, topography transitions from smooth to dots and from dots to ripples are observed with increasing U_{acc}. At low U_{acc} (absolute values smaller than −400 V) independent of α_{ion} the surface remains smooth, and with increasing α_{ion} this parameter region increases to larger absolute values of U_{acc} until the surface topography is not affected by U_{acc}. The boundaries (dotted lines) in the TD are guides for the eyes used to distinguish between different topography regions similar to the TD E_{ion} versus α_{ion} (see section 4).

In this way investigations were also performed for Si (figure 28) using the same sputtering conditions as for Ge. Here topographical transitions are also observed: however, the boundary positions between different parameter regions vary compared to Ge. This may be related to the different masses of target atoms. The TD in figure 28 shows that the topography is stable with respect to U_{acc} for small ion incidence angles. However, at angles between 20° and 40° topographical transitions are present. For example, at $\alpha_{ion} = 35°$ a transition from smooth to dot to a ripple + dot structure with increasing absolute value of U_{acc} is observed. It is important to state that these topography transitions are continuous. Thus, between the ripple and dot parameter regions, there is an intermediate region where ripples and

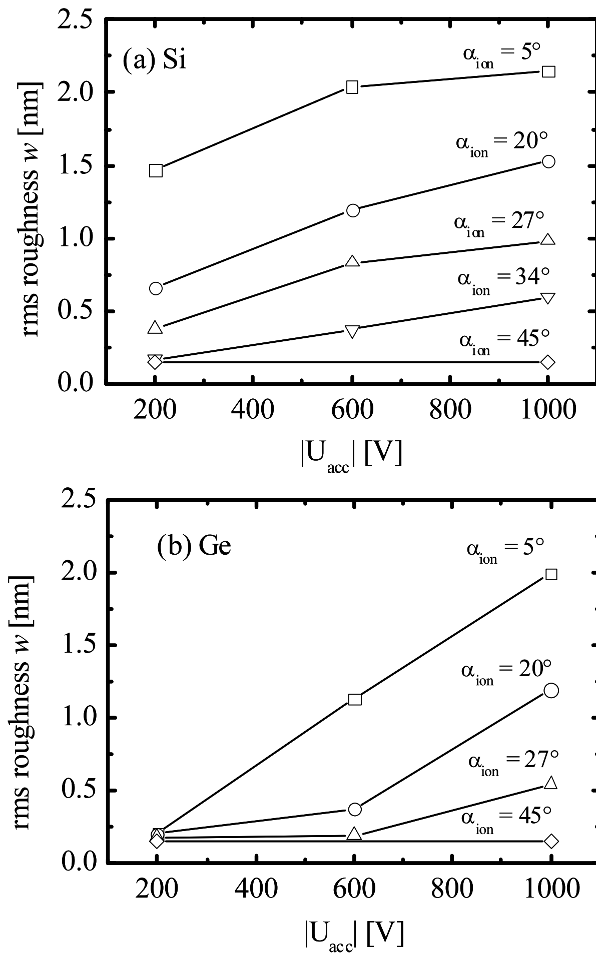

Figure 29. The dependence of surface roughness on U_{acc}, deduced from the experimental data presented in the topography diagrams. The results are plotted for different α_{ion}: (a) Si, (b) Ge.

dots coexist together. Passing from a parameter region where structures form to a smooth one the amplitude of structures decreases gradually until the surface remains smooth.

The relationship between the structure amplitude and U_{acc} are summarized in figure 29 for Si and Ge surfaces. The results are presented for different α_{ion}. In general, an increase of the surface roughness with increasing absolute value of U_{acc} for both materials is observed, except for $\alpha_{ion} = 45°$ where the surface topography is independent of U_{acc}. In the case of Ge, for all incidence angles the surface roughness takes the same value for $U_{acc} = -200$ V. Overall, the surface roughness decreases with ion incidence angle. It is worth mentioning that the periodicity of nanostructures remains constant with varying U_{acc}.

Finally, the acceleration voltage is an important parameter also for the formation of dot patterns in the case with sample rotation. An example is given in figure 30, where AFM images showing the surface topography after Kr^+ ion beam sputtering of Si surfaces, at grazing incidence with $U_{acc} = -200$ and -1000 V, are depicted. In this case, U_{acc} has an impact on the lateral ordering of dots, i.e. with increasing U_{acc} the ordering of dots is improved, visible in the AFM image.

The above discussion underlines the importance of the internal ion beam parameters on the surface topography. By varying the beam characteristics, different topographies can form on the surface. One important conclusion from the above results is the use of U_{acc} as an additional parameter during the sputtering process for controlling the resulting surface topography. The influence of U_{acc} is not only characteristic of Si and Ge surfaces; an influence of U_{acc} was also found on III/V semiconductors [54]. The observed dependence of the structure formation on U_{acc}, i.e. angular distribution of ions, is unique to the broad beam ion source used. Other ion sources with other extraction system geometries probably will produce other structure properties and dependences.

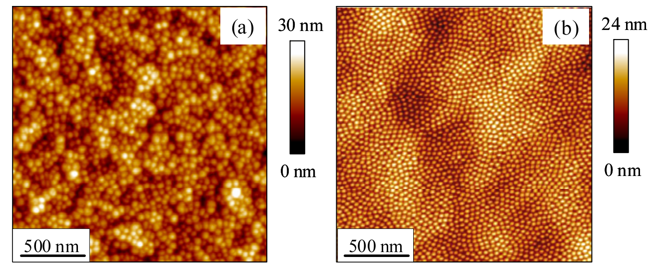

Figure 30. AFM images of Si surfaces after sputtering with Kr^+ ions at $E_{ion} = 1000$ eV, $\alpha_{ion} = 75°$, $\Phi = 6.7 \times 10^{18}$ cm^{-2}. (a) $U_{acc} = -200$ V, (b) $U_{acc} = -1000$ V.

At the end, it is worth mentioning that the above discussion would explain the different results obtained from different research groups (and the difficulty in reproducing these results) for nanostructures on Si and Ge surfaces [55–59].

To come to a comprehensive understanding of the impact of such internal ion beam properties on the structure formation more detailed experimental investigations are necessary. Currently we follow different approaches for a more quantitative analysis of the angular distribution. In this regard the influence of other parameters affecting the angular distribution of ions will also be studied in detail, like the plasma density, grid inter-distance or the geometrical set-up ion optical system versus sample holder.

6. Summary

In this review a systematic experimental study of the surface topography evolution on Si and Ge surfaces during low-energy ion beam erosion is presented. It was demonstrated that ion beam erosion at low ion energies up to 2000 eV is very well suited for producing nanostructured surfaces. Due to self-organization processes, and for given sputtering conditions, these nanostructures can show an almost perfect lateral ordering covering the whole sample area under treatment. In this context a particular interest is given to the formation of ripple and dot nanostructures on the surface. During the experimental investigations it was shown that there are a large number of process parameters that influence the evolution of the surface topography. Explicitly, a thorough study of the role of ion incidence angle, ion energy and ion fluence on the evolution of ripples and dots is performed. These patterns are analysed in terms of surface roughness and wavelength (mean size) of nanostructures. Ion incidence angle investigations, for

the case without sample rotation, show ripple patterns with the wavevector parallel to the ion beam projection evolving on the surface at near-normal ion incidence. However, experimental studies indicate no change in orientation of ripples with increasing ion incidence angle. Furthermore, a detailed study shows transitions between ripples and dots by fine variations of ion incidence angle. This behaviour is similar for both materials, Si and Ge.

The wavelength (mean size) of nanostructures can be controlled up to a certain range by varying the ion energy from 500 up to 2000 eV, and in fact increases with increasing ion energy. In this way the wavelength (mean size) of nanostructures can be varied between 30 and 70 nm. At the same time, the nanostructures maintain their lateral ordering. Temporal investigations of the evolution of ripples and dots showed that lateral ordering of nanostructures increases with increasing ion fluence, while the wavelength of nanostructures remains constant with ion fluence. The independence of the wavelength with ion fluence is observed at different sputtering conditions. In the context of this work the influence of ion mass (Ne^+, Ar^+, Kr^+ and Xe^+ ions) on the surface evolution process is also investigated. In general, in order that pattern formation occurs the incoming ion should have at least a certain mass compared to the target material. Thus, no patterns evolve on Si using Ne^+ ions and for Ge using Ne^+ and Ar^+ ions. However, once ripples and dots evolve on the surface their dynamics (wavelength, height, lateral ordering) is not influenced by the ion mass. Similar dependences are observed also for dot structures evolving on Si surfaces at grazing ion incidence with sample rotation. In addition, this work shows that internal ion beam parameters, characteristic for broad beam ion sources, are also crucial for the formation of nanostructures at least on semiconductor materials. Explicitly, the role of the acceleration voltage applied on the second grid of broad beam ion sources that influences the angular distribution of ions within the beam and the beam divergence is studied. This parameter is important for: (i) the evolution of nanostructures on the surface and (ii) the lateral ordering of nanostructures. In this way, an additional parameter for controlling the process of nanostructure formation is introduced.

Another important result is that by combining the internal ion beam parameter with the ion incidence angle, at certain sputtering conditions, parameter regions are identified where transitions between ripples and dots, or vice versa, exist. In particular, the transition from ripples to dots is of particular importance. Due to the previous existence of ripples the evolving dots have an almost perfect lateral ordering covering the whole sample area.

Besides the extensive experimental work summarized in this review, there is still much to be done. As already stated the parameters that are less studied or not studied at all, as shown above, are the internal beam parameters which are very important for the formation of patterns. This would include simulations of the beam profile for the given experimental data as stated in section 5. Also investigation of the geometrical set-up of the ion source should be studied.

Overall, these investigations show that ion beam sputtering is very well suited as an alternative method to produce large area nanostructures on the surface. Although the process itself is a stochastic one the evolving topographies show a remarkably high lateral ordering. The formation of patterns on Si and Ge surfaces and previous reports on III/V semiconductors show that this process is a general one. However, the adjustment of the sputtering conditions to the particular material is very important.

The simple one-step process of nanostructure formation with the possibility of large scale patterning makes low-energy ion beam erosion a very attracting tool for applications in different fields of nanotechnology. Promising applications are in the field of optoelectronics, used as templates for metallic nanostructures, e.g. for high-density storage. A straightforward application is in the field of optics for structuring of optical materials that can be used as passive optical elements. Another application is hierarchical micro- and nanostructuring for functional optical surfaces. In this case conventional lithographical methods can be merged with ion-beam-induced self-organization processes [60, 61] which facilitates: (i) producing new types of nanostructures, (ii) having better control on the position of a certain type of nanostructures and (iii) the possibility to structure curved surfaces.

Acknowledgments

The authors would like to express their gratitude to many colleagues for their help during the years. In particular: H Neumann, M Tartz, F Scholze, B Faust for the very useful discussions concerning broad beam ion sources, especially M Tartz for characterizing the ion beam, i.e. performing the simulations; T Höche (HRTEM), R Fechner and A Schindler (ion beam smoothing), D Flamm (technical support); G Carbone and T H Metzger for their support in performing the GISAXS and GID measurements at the beamline ID01 at ESRF. The authors appreciate M J Aziz, P Brenner, G Bola, E Chason, R Cuerno and their participating colleagues of the research group FOR 845 for their enlightening discussions. Also appreciated is the financial support from the Deutsche Forschungsgemeinschaft FOR 365, FOR 1476 and FOR 845.

References

[1] Haymann P 1959 *C. R. Acad. Sci.* **248** 2472
[2] Behner H and Wedler G 1985 *Surf. Sci.* **160** 271
[3] Carter G, Nobes M J and Whitton J L 1985 *Appl. Phys.* A **38** 77
[4] Rusponi S, Boragno C and Valbusa U 1997 *Phys. Rev. Lett.* **78** 2795
[5] Murty M V R, Curcic T, Judy A, Cooper B H, Woll A R, Brock J D, Kycia S and Headrick R L 1998 *Phys. Rev. Lett.* **80** 4713
[6] van Dijken S, de Bruin D and Poelsema B 2001 *Phys. Rev. Lett.* **86** 4608
[7] Malis O, Brock J D, Headrick R L, Yi M S and Pomeroy J M 2002 *Phys. Rev.* B **66** 035408
[8] Chan W L, Pavenayotin N and Chason E 2004 *Phys. Rev.* B **69** 245413
[9] Carter G, Nobes M J, Paton F, Williams J S and Whitton J L 1977 *Radiat. Eff. Defects Solids* **33** 65

[10] MacLaren S W, Baker J E, Finnegan N L and Loxton C M 1992 *J. Vac. Sci. Technol.* A **10** 468
[11] Elst K, Vandervorst W, Alay J, Snauwaert J and Hellemans L 1993 *J. Vac. Sci. Technol.* B **11** 1968
[12] Malherbe J B 1994 *CRC Crit. Rev. Solid State Mater. Sci.* **19** 55
[13] Chason E, Mayer T M, Kellerman B K, McIlroy D T and Howard A J 1994 *Phys. Rev. Lett.* **72** 3040
[14] Carter G and Vishnyakov V 1995 *Surf. Interface Anal.* **23** 514
[15] Vajo J J, Doty R E and Cirlin E H 1996 *J. Vac. Sci. Technol.* A **14** 2709
[16] Vijaya Sankar K, Demanet C M, Malherbe J B, van der Berg N G and Odendaal R Q 1996 *Surf. Interface Anal.* **24** 497
[17] Jiang Z X and Alkemade P F A 1998 *Appl. Phys. Lett.* **73** 315
[18] Erlebacher J, Aziz M J, Chason E, Sinclair M B and Floro J A 1999 *Phys. Rev. Lett.* **82** 2330
[19] Ziberi B, Frost F, Höche Th and Rauschenbach B 2005 *Phys. Rev.* B **72** 235310
Muñoz-Garcìa J, Vázquez L, Cuerno R, Sánchez-García J A, Castro M and Gago R 2007 arXiv:0706.2625v1
Keller A, Rossbach S, Facsko S and Möller W 2008 *Nanotechnology* **19** 135303
[20] Facsko S, Dekorsy T, Koerdt C, Trappe C, Kurz H, Vogt A and Hartnagel H L 1999 *Science* **285** 1551
[21] Frost F, Schindler A and Bigl F 2000 *Phys. Rev. Lett.* **85** 4116
[22] Gago R, Vazquez L, Cuerno R, Varela M, Ballesteros C and Albella J M 2001 *Appl. Phys. Lett.* **78** 3316
[23] Ziberi B, Frost F, Höche T and Rauschenbach B 2005 *Appl. Phys. Lett.* **87** 033113
[24] Umbach C C, Headrick R L and Chang K C 2001 *Phys. Rev. Lett.* **87** 246104
[25] Habenicht S, Bolse W, Lieb K P, Reimann K and Geyer U 1999 *Phys. Rev.* B **60** R2200
[26] Wu Y-R, Datta A and Wang Y L 2001 *Phys. Rev.* B **63** 125407
[27] Frost F, Ziberi B, Höche T and Rauschenbach B 2004 *Nucl. Instrum. Methods* B **216** 9
[28] Carter G and Vishnyakov V 1996 *Phys. Rev.* B **54** 17647
[29] Chini T K, Sanyal M K and Bhattacharyya S R 2002 *Phys. Rev.* B **66** 153404
[30] Hazra S, Chini T K, Sanyal M K, Grenzer J and Pietsch U 2004 *Phys. Rev.* B **70** 121307(R)
[31] Gago R, Vázquez L, Plantevin O, Metzger T H, Muñoz-Garcia J, Cuerno R and Castro M 2006 *Appl. Phys. Lett.* **89** 233101
[32] Ziberi B, Frost F and Rauschenbach B 2006 *Appl. Phys. Lett.* **88** 173115
[33] Carbonne D, Alija A, Plantevin O, Gago R, Facsko S and Metzger T H 2008 *Nanotechnology* **19** 035304
[34] Ziberi B, Frost F, Tartz M, Neumann H and Rauschenbach B 2008 *Appl. Phys. Lett.* **92** 063102
[35] Ziberi B 2007 *Ion Beam Induced Pattern Formation on Si and Ge Surfaces* (Leipzig: Engelsdorfer)
[36] Tartz M 2003 *PhD Thesis* University of Leipzig
[37] Zhao Y, Wang G-C and Lu T-M 2001 *Characterization of Amorphous and Crystalline Rough Surfaces: Principles and Applications* (San Diego, CA: Academic)
[38] Frost F, Fechner R, Ziberi B, Flamm D and Schindler A 2004 *Thin Solid Films* **459** 100
[39] Frost F, Fechner R, Flamm D, Ziberi B, Frank W and Schindler A 2004 *Appl. Phys.* A **78** 651
[40] Frost F, Fechner R, Ziberi B, Völlner J and Schindler A 2009 *J. Phys.: Condens. Matter* **21** 224026
[41] Carter G, Vishnyakov V, Martynenko Y V and Nobes M J 1995 *J. Appl. Phys.* **78** 3559
[42] Biersack J P, Ziegler F and Littmark U 1985 *The Stopping and Range of Ions in Solids* (New York: Pergamon)
[43] Gnaser H 1999 *Low-Energy Ion Irradiation of Solid Surfaces* (Berlin: Springer)
[44] Frost F and Ziberi B 2009 in preparation
[45] Bradley R M 1996 *Phys. Rev.* E **54** 6149
[46] Makeev M A, Cuerno R and Barabasi A L 2002 *Nucl. Instrum. Methods* B **197** 185
[47] Tartz M, Hartmann E, Deltschew R and Neumann H 2002 *Rev. Sci. Instrum.* **73** 928
[48] Zeuner M, Neumann H, Scholze F, Flamm F, Tartz M and Bigl F 1998 *Plasma Sources Sci. Technol.* **7** 252
[49] Kaufman H R, Cuomo J J and Harper J M E 1982 *J. Vac. Sci. Technol.* **21** 725
[50] Kaufman H R and Robinson R S 1982 *AIAA J.* **20** 745
[51] Korzec D, Schmitz K and Engemann J 1988 *J. Vac. Sci. Technol.* B **6** 2095
[52] Ray M A, Barnett S A and Greene J E 1989 *J. Vac. Sci. Technol.* A **7** 125
[53] Becker R and Herrmannsfeldt W B 1992 *Rev. Sci. Instrum.* **63** 2756
[54] Ziberi B, Frost F, Tartz M, Neumann H and Rauschenbach B 2004 *Thin Solid Films* **459** 106
[55] Fan W, Lin L, Qi L-J, Li W-Q, Sun H-T, Gu Ch, Zhao Y and Lu M 2006 *J. Phys.: Condens. Matter* **18** 3367
[56] Gago R, Vazquez L, Cuerno R, Varela M, Ballesteros C and Albella J M 2002 *Nanotechnology* **13** 304
[57] Kim J, Cahill D G and Averback R S 2003 *Phys. Rev.* B **67** 045404
[58] Ludwig F, Eddy C R, Malis O and Headrick R L 2002 *Appl. Phys. Lett.* **81** 2770
[59] Van Nostrand J E, Chey S J and Cahill D G 1998 *Phys. Rev.* B **57** 12536
[60] Cuenat A, George H B, Chang K-C, Blakely J M and Aziz M J 2005 *Adv. Mater.* **17** 2845
[61] Frost F, Ziberi B, Schindler A and Rauschenbach B 2008 *Appl. Phys.* A **91** 551–9